DOE/ER/40293--4

DE90 009470

Middle Tennessee State University

NUCLEAR STRUCTURE STUDIES *via* NEUTRON INTERACTIONS

Progress Report
1 July 1989 – 30 June 1990

Robert F. Carlton
Principal Investigator
Dept. of Chemistry & Physics

Ramona Rice, Director
Budget & Systems Planning

Middle Tennessee State University
Murfreesboro, Tennessee 37132
March 1990

Prepared for
THE U.S. DEPARTMENT OF ENERGY
Under Contract No. DE-FG05-86ER40293

NOTICE

ABSTRACT

Research performed consisted of: (1) refinement of previous analysis of high resolution total cross sections for n + ^{40}Ar in an effort to remove some ambiguities in J^{π} assignments and completion of two papers dealing with this analysis and a companion theoretical treatment of the associated scattering functions and R-functions; (2) extension of the analysis of neutron total cross section data on ^{48}Ca to 3.5 MeV in neutron energy and modeling of the results with a dispersive optical model based on parameters from ^{40}Ca scattering data; (3) attempted improvement of spin and parity assignments for data on ^{122}Sn and determination of external R-function parameters; (4) development of a graphical interface, coupled with a code for calculation of R-matrix based total cross sections and parameter minimization, for an MS-DOS-based microcomputer.

I. Introduction

Efforts during the reporting period have been directed toward developing a graphical interface for the 386 microcomputer to be incorporated with a previously developed code for calculating neutron total cross sections in the R-matrix formalism. In addition a minimization component has been added to the calculation routines. This greatly enhances the ability to analyze an isotope with greater attention to the details of spin and parity and with greater speed. This has eliminated the continual switching between calculations and parameter-file modification previously required and rendered the analysis completely screen interactive through a mouse.

This tool has been used to analyze a data set (^{48}Ca) which had almost been abandoned due to complex overlapping structures in the cross section above 2.0 MeV. Parameters of the R-matrix formulation have been obtained in preparation for comparison to predictions of a dispersive optical model. A paper is in preparation which incorporates experimental and theoretical details of this interaction and should be complete by the end of the reporting period..

Finally, attention has been directed to completion of the experimental analysis of the n$-^{40}$Ar system in the R-matrix formalism. These results have been compared to predictions of a dispersive optical model with parameters deduced from available data on n$-^{40}$Ca. This work will have been submitted for review before the end of the reporting period.

II. The n $-$ ^{40}Ar System

The n$-^{40}$Ar system has been investigated through total cross section measurements over the energy range 10 keV to 40 MeV. Detailed resonance analysis has been performed up to 1.5 MeV. From this analysis we have obtained average scattering functions and external R-functions of the the R-matrix formalism, for individual partial waves. While these data represent a minuscule wealth of data compared to scattering measurements, for purposes of deducing optical model parameters, no other type of measurement provides such clear information on the scattering of individual partial waves.

The results of the analysis are dedicated to a dispersive optical model potential for the

$n-^{40}Ar$ system in the sense that the model parameters based on extensive data for the $n-^{40}Ca$ system have been used, with suitable corrections, to model the results of the present analysis.

III. Dispersive Optical Model Analysis

Collaborators: C.H. Johnson & R.R. Winters

A dispersive component to the optical model potential is obtained from a dispersion relation which connects the real to the imaginary part of the mean field. This provides for a unified description of both the optical model potential at positive energies and the shell model potential in the bound region. This is realized by the inclusion in the dispersive term of the effect of coupling of the single particle degree of freedom to low-lying core excitations. The complicated energy dependence of the real potential for low and negative energies is thereby achieved.

A definitive dispersive optical model analysis (DOMA) requires extensive differential scattering data. Such data are available[1-3] for neutron scattering from ^{40}Ca, ^{90}Zr, and ^{208}Pb, each of which have a closed neutron shell. In the case of the $n-^{40}Ca$ analysis[4], which is of particular interest here, the experimental data included (a) the total cross section for neutron energies from 1 to 80 - MeV, (b) differential cross sections at fourteen neutron energies from 5 to 40 - MeV, (c) analyzing powers for five energies from 10 to 17 - MeV, and (d) single-particle bound state energies, not only for the valence shells but also for deeply bound states down to -66 MeV.

The DOMA is not possible for the $n-^{40}Ar$ system because no scattering data are available. The parameters from the DOMA for $n-^{40}Ca$ can be reasonably be extended to the $n-^{40}Ar$ system by correcting for the shift in the Fermi energy and for the contribution of the isovector potential to $n-^{40}Ar$. The comparison of the two systems yields an empirical isovector potential which is not confused by mass dependencies because the two nuclei are isobars. The effect of the isovector potential is relatively large because they differ significantly in their asymmetry coefficients. In fact no other pair of isobars for $A > 40$ has such a large difference.

Data are available for $n-^{40}Ar$ in the form of bound state structure information[5], total cross section for $E < 40$ MeV[6], and R-matrix resonance parameters for $E < 1.5$ MeV[6]. The total cross sections alone are meager data in comparison to extensive scattering data listed

above for neutrons on ^{40}Ca. Moreover, counting statistical uncertainties are large for the 20- to 40-MeV total cross section for ^{40}Ar. The R-matrix resonance parameters however provide us with scattering functions for individual partial waves at low energies. This information may prove useful in explaining the failure of a simple dispersive optical model to explain the total cross section of both ^{40}Ca and ^{40}Ar without recourse to orbital angular momentum dependence and/or an energy dependence of the shape parameters of the potential.

IV. Description of the Model

The model is formulated in terms of a Fermi-shifted energy,

$$\mathcal{E} = E - E_f \qquad 1$$

rather than the normal incident neutron energy E. The mean field is expressed,

$$\mathcal{M}(r;\mathcal{E}) = \mathcal{V}(r;\mathcal{E}) + i\mathcal{W}(r;\mathcal{E}), \qquad 2$$

with the real part being the sum of a local equivalent to the Hartree-Fock (HF) potential and $\Delta\mathcal{V}$ being the dispersive contribution,

$$\mathcal{V}(r;\mathcal{E}) = \mathcal{V}_H(r;\mathcal{E}) + \Delta\mathcal{V}(r;\mathcal{E}) \ . \qquad 3$$

In addition to the central component there is a spin-orbit contribution to the mean field which is assumed to be real and have the standard form;

$$\mathcal{V}_{so}(r;\mathcal{E}) = \vec{\sigma}\cdot\vec{\ell}\,(\tfrac{\hbar}{m_\pi c})\,V_{so}\tfrac{1}{r}\,\tfrac{d}{dr}\,f(X_{so})\ , \qquad 4$$

with energy-independent parameters $V_{so} = 5.40$ MeV, $r_{so} = 1.02$ fm, and $a_{so} = 0.50$ fm. The HF potential is assumed the have the Woods-Saxon form with shape parameters that are energy independent;

$$\begin{aligned} \mathcal{V}_H(r;\mathcal{E}) &= V_H(\mathcal{E})\cdot f(X_H), \\ f(X_H) &= [\,1 + \exp(X_H)\,]^{-1}, \\ X_H &= (\,r - R_H)/a_H, \\ R_H &= r_H\cdot A^{1/3}. \end{aligned} \qquad 5$$

The energy dependence of the central depth of the real part of the potential has linear and exponential components according to :

$$\begin{aligned} V_H(\mathcal{E}) &= V_H(0) + \alpha\mathcal{E} && \text{for } \mathcal{E} < 0, \\ V_H(\mathcal{E}) &= V_H(0)\cdot\exp[\alpha\mathcal{E}/V_H(0)] && \text{for } \mathcal{E} > 0. \end{aligned} \qquad 6$$

The dispersion relation is used to connect the dispersive component to the imaginary potential;

$$\Delta\mathcal{V}(r;\mathcal{E}) = \frac{P}{\pi}\int_{-\infty}^{\infty}\frac{\mathcal{W}(r;\mathcal{E}')d\mathcal{E}'}{(\mathcal{E}'-\mathcal{E})} \quad , \tag{7}$$

where P denotes the principal value integral. The integral is evaluated assuming $\mathcal{W}(r;\mathcal{E}')$ to be symmetric with respect to the Fermi energy. The imaginary field, $\mathcal{W}$, is the sum of surface and volume components,

$$\mathcal{W}(r;\mathcal{E}) = \mathcal{W}_V(r;\mathcal{E}) + \mathcal{W}_S(r;\mathcal{E}), \tag{8}$$

where the volume component is assumed to have the same shape as the HF field. The shape of the imaginary component is taken to be the radial derivative of a Woods-Saxon form with energy-independent shape parameters r_S and a_S;

$$\mathcal{W}_S(r;\mathcal{E}) = -4\, a_S \cdot W_S(\mathcal{E})\frac{d}{dr}f(X_S). \tag{9}$$

With the shapes of both components of the imaginary potential being energy independent, the dispersive terms will have the same shapes as the corresponding imaginary parts and are given by integrals involving only the well depths;

$$\Delta V_x(\mathcal{E}) = \frac{P}{\pi}\int_{-\infty}^{\infty}\frac{W_x(\mathcal{E}')d\mathcal{E}'}{(\mathcal{E}'-\mathcal{E})} \quad , \tag{10}$$

where "x" denotes either surface or volume, "s" or "v". Since the shape of the volume component, $\mathcal{W}_V(r;\mathcal{E})$, is assumed to be the same as for the HF potential, the total real volume potential $\mathcal{V}(r;\mathcal{E})$ will involve a simple sum of well depths;

$$\mathcal{V}_V(r;\mathcal{E}) = V_V(\mathcal{E})\cdot f(X_H) \tag{11}$$

where

$$V_V(\mathcal{E}) = V_H(\mathcal{E}) + \Delta V_V(\mathcal{E}). \tag{12}$$

The DOMA applied to ^{40}Ca yielded best-fit values for nine free parameters associated with the HF potential and the shape and depth parameters of the real potential. In addition,

two parameters associated with the imaginary volume potential were found. The results are given in the following table:

$r_H = 1.18$ fm	$a_H = 0.70$ fm
$r_s = 1.26$ fm	$a_s = 0.60$ fm
$V_H^{Ca}(0) = -58.8$ MeV	$\alpha^{Ca} = 0.55$
$W_v^{\infty} = -14.6$ MeV	$\mathcal{E}_v = 130$ MeV
$W_S^{\infty} = -8.7$ MeV	$\mathcal{E}_{S1} = 15$ MeV
$\mathcal{E}_{S2} = 130$ MeV	

13

In order to address ^{40}Ar in this formulation we assume the two systems have the same shape parameters, since the two nuclei are isobars. The same depths are assumed for the surface and volume imaginary depths. The remaining parameters for the specialization to ^{40}Ar are those parameterizing the HF potential. The depth, $V_H^{Ar}(0)$, of this potential at the Fermi energy is deduced from the observed energies of the particle and hole states in the valence shells, utilizing energies and spectroscopic factors from the most recent literature[7,8]. These are summarized in Table I.

The Fermi energy lies between the ground states of ^{39}Ar and ^{41}Ar. Both ground states have $J^{\pi} = 7/2^-$, but neither energy is that of the $1f_{7/2}$ orbit because of the presence of the $(1f_{7/2})^2$ neutron pair in ^{40}Ar. In Table I we denote the ^{41}Ar ground state by "$(f_{7/2})^2 + f_{7/2}$" to indicate that it is formed by addition of an $f_{7/2}$ neutron to the $(1f_{7/2})^2$ pair. In like manner, the notation "$(f_{7/2})^2 - f_{7/2}$" for the ^{39}Ar ground state indicates that it is formed by pickup of one of the paired neutrons. The 3.8-MeV energy difference shows that the pairing energy is large. The exact location of E_F between the ground states was found not to be critical to the analysis. We take it to be midway between the states;

$$E_F = -8.0 \text{ MeV} \qquad \text{for n}-^{40}\text{Ar}.$$

The Fermi energy and the level energies from Table I are represented in Fig. 1 by the diagram "EXPT" for n-^{40}Ar. In keeping with the above discussion, the ground states are represented by dashed lines and labeled $7/2^-$ rather than $1f_{7/2}$. The other levels are labeled as single-particle or single-hole states. By choosing these energies, we make the tacit assumption that

the particle or hole states are reached by stripping or pickup without disturbing the paired $f_{7/2}$ neutrons in the ^{40}Ar core, and we justify that approximation by the fact that the two $f_{7/2}$ particles have a large pairing energy. At the left in the figure are plotted the empirical and predicted structures for the same levels for n-^{40}Ca, adopted from Fig. 12 of Ref. 4. We see the corresponding states for n-^{40}Ca are bound much deeper than for n-^{40}Ar. This was already apparent from the 4-MeV difference in the Fermi energies. Clearly, the HF depth, $V_H^{Ar}(0)$, for n-^{40}Ar must be somewhat less negative than the depth $V_H^{Ca}(0)$ for n-^{40}Ca.

Essentially, two sets of data are required to determine the two parameters, $V_H^{Ar}(0)$ and α^{Ar}. For one set we take the energies from Table I for the $2p_{1/2}$, $2p_{3/2}$, $2s_{1/2}$, and $1d_{3/2}$ bound states. For the other we take the total cross section for neutron energies from 11 to 40 MeV. To first order we choose the depth $V_H^{Ar}(0)$ to fit the bound states and then choose the energy coefficient α^{Ar} to fit the total cross section. Actually, we must iterate these steps to obtain the best overall fit. For the following more detailed description of the iterations, we present figures based on our final parameters. These are

$$\begin{aligned} V_H^{Ar}(0) &= -53.2 \pm 0.55 \text{ MeV} \\ \alpha^{Ar} &= 0.39 \pm 0.05 \end{aligned} \qquad 14$$

The remaining parameters of the DOMA were taken from the n-^{40}Ca analysis of Ref. 4 and listed above. The bound-state structure predicted by the real part of the model is represented by the right-hand diagram in Fig. 1. It agrees well with the observed structure. In particular, it is compressed in energy relative to that of ^{40}Ca. This is a consequence of the smaller value for α^{Ar}.

We now describe in more detail the evaluation of $V_H^{Ar}(0)$ and its uncertainty. The curve in Fig. 2a represents the depth $W_S(\mathcal{E})$ for the imaginary surface potential of the model and the curve in Fig. 2b represents the corresponding real dispersive potential $\Delta V_S(\mathcal{E})$.

In Fig. 3 the curve represents the total cross section predicted from our model and the symbols represent the measured values averaged over appropriate energy intervals. The vertical heights of the symbols represent the uncertainties from counting statistics. The energy coefficient α^{Ar} has been chosen to yield a good fit for $E > 11$ MeV. Indeed, the model curve agrees well with the data for $11 < E < 40$ MeV but is too high for $2 < E < 11$ MeV.

Fig. 4 shows the total cross sections for ^{40}Ca. We see similarly that for $E < 9.5$ MeV the original DOMA for n$-^{40}$Ca exhibits a discrepancy. It was this common discrepancy that

prompted us to ignore the total cross sections for E < 11 MeV in our fitting procedure. Essentially, that region was ignored also for most of the ^{40}Ca analysis, being only a small part of the very broad energy range of the analysis.

V. Isovector Potential.

Empirical analyses showed that the central HF depth is shallower for n$-^{40}$Ar than for n$-^{40}$Ca. This is because the real part of the symmetry potential contributes for ^{40}Ar but not for ^{40}Ca and it has the opposite sign from the HF potential. The ^{40}Ar nucleus is asymmetric with 18 protons and 22 neutrons, whereas ^{40}Ca is symmetric with 20 each. Thus for ^{40}Ar the asymmetry coefficient is

$$\eta = (N - Z)/A = 0.10. \qquad 15$$

The energy variable $\mathcal{E}$ is well suited for introducing the effect of the symmetry potential. From the discussion in Ref. 4 we have

$$\eta\, V_1^H(\mathcal{E}) = V_H^{Ar}(\mathcal{E}) - V_H^{Ca}(\mathcal{E}), \qquad 16$$

where $V_1^H(\mathcal{E})$ is the HF approximation to the central depth of the symmetry potential. The empirical parameters required for the right-hand side of Eq. 15 are given by Eq. 12. The resulting symmetry potential is represented by the solid curve in Fig. 5. The vertical symbol at $\mathcal{E} = 0$ represents the estimated uncertainty propagated from that given in Eq. 13 and the symbol at $\mathcal{E} = 33$ MeV represents the uncertainty which is propagated for the general region from the coefficient in Eq. 13. The latter value is large because of the large statistical uncertainties in the total cross sections in Fig. 3.

The dashed curve in Fig. 5 represents the symmetry potential that was deduced for n$-^{40}$Ca in Ref. 4 by comparison of the HF potential with that previously deduced[9] for n$-^{208}$Pb;

$$\eta\, V_1^H(\mathcal{E}) = V_H^{Pb}(\mathcal{E}) - V_H^{Ca}(\mathcal{E}), \qquad 17$$

where $\eta = 0.21$ for ^{208}Pb. The solid and dashed curves are in good agreement.

VI. Dispersive Optical Model in the Resonance Region.

The primary motivation of the high resolution measurements was to resolve resonances in

the neutron total cross section for energies below the inelastic threshold at 1.5 MeV. The R-matrix provides us with detailed descriptions of the neutron scattering functions for the $s_{1/2}$, $p_{1/2}$ and $p_{3/2}$ partial waves for the energy domain $[E_\ell, E_u]$ from $E_\ell = 0.0$ MeV to $E_u = 1.5$ MeV. Here we compare the energy averages of those functions to the optical model predictions for the same partial waves.

Since only the entrance neutron channel is important for the domain $[E_\ell, E_u]$, the R-matrix reduces to an R-function which, for the total angular momentum $j = \ell \pm \frac{1}{2}$, reads

$$S_{\ell j}(E) = e^{-2\phi_\ell(E)} \cdot \frac{1 + iP_\ell(E)\, R_{\ell j}(E)}{1 - iP_\ell(E)\, R_{\ell j}(E)} , \qquad 18$$

where $P_\ell(E)$ and $\phi_\ell(E)$ are the penetrability and the hard-sphere phase shift evaluated at the channel radius a_c. The value of a_c is arbitrary, except that it should be near the nuclear radius. Once chosen, however, it should be used in both the data analysis and optical model predictions. We have used a value of 5.0 fm. The R-function, $R_{\ell j}(E)$, is a sum over the n - resonances with quantum numbers ℓ and j that are observed within the domain $[E_\ell, E_u]$, plus an external R-function which accounts for the influence of levels outside the domain;

$$R_{\ell j}(E) = \sum_{\lambda=1}^{n} \frac{\gamma^2_{\ell j \lambda}}{E_{\ell j \lambda} - E} + R^{ext}_{\ell j}(E) , \qquad 19$$

where $E_{\ell j \lambda}$ and $\gamma^2_{\ell j \lambda}$ are the energy and reduced width of the λth level. In Fig. 6 the data points represent values of $R^{ext}_{\ell j \lambda}(E)$ deduced at six energies where the resonance-potential interference patterns gave the small uncertainties represented by the vertical heights of the symbols. In Fig. 7 the "staircases" represent cumulative sums of reduced widths up to the neutron energy E. Each riser is a reduced width, $\gamma^2_{\ell j \lambda}$, and each tread is the spacing between adjacent levels. The error bar at the top of each staircase corresponds to the fractional uncertainty, $\sqrt{(2/n)}$, for a sum of n widths drawn from a Porter-Thomas distribution.

The energy dependence of the empirical scattering function from Eq. 17 is very complicated. To compare with the model predictions we must first average over energy. Good agreement between model and experiment requires that the model scattering function be approximately equal to the smoothed experimental average;

$$S^{OM}_{\ell j}(E) = \langle S_{\ell j}(E) \rangle . \qquad 20$$

The energy averaging could be done numerically. It has been shown[10] that comparison of the model to the experimental average can be accomplished by a simple prescription. To utilize that prescription we expand the model scattering function in the same form as for the experimental scattering function, using the same channel radius;

$$S^{OM}_{\ell j}(E) = e^{-2\phi_\ell(E)} \cdot \frac{1 + iP_\ell(E)\, \Re^{OM}_{\ell j}(E)}{1 - iP_\ell(E)\, \Re^{OM}_{\ell j}(E)} , \qquad 21$$

with

$$\Re^{OM}_{\ell j}(E) = R^{OM}_{\ell j}(E) + i\,\pi \cdot s^{OM}_{\ell j}(E) . \qquad 22$$

Then we can use the following simple prescription for comparing the model functions to the averaged empirical functions;

$$\sum_{\lambda=1}^{k} \gamma^2_{\ell j \lambda} \simeq \int_{E_\ell}^{E_k} s^{OM}_{\ell j}(E')\, dE'), \qquad 23$$

and

$$R^{ext}_{\ell j}(E) \simeq R^{OM}_{\ell j}(E) - P \int_{E_\ell}^{E_u} \frac{s^{OM}_{\ell j}(E')\, dE')}{(E' - E)} , \qquad 24$$

where P denotes the principal value integral. The left-hand sides of these two equations are presented in Figs. 6 and 7 and the optical model predictions from the right-hand sides are represented by the curves in those figures.

The predicted curves in Figs. 6 and 7 agree relatively well with the data. Both model and experiment show R^{ext} to be much more positive for s-waves than for p-waves. This is because the $3s_{1/2}$ state is unbound whereas the $2p_{1/2}$ and $2p_{3/2}$ states are bound. Also the $s_{1/2}$ strength is relatively large because the $3s_{1/2}$ state is only slightly unbound. FInally the spin-orbit potential makes the strength function larger and R^{ext} more negative for $p_{1/2}$ than for $p_{3/2}$ because the $2p_{1/2}$ state is bound less deeply than the $2p_{3/2}$ state.

As can be seen, there are some discrepancies outside the experimental uncertainties. For p-waves, the predicted strength functions are too large and the R^{ext} for $p_{1/2}$ is too negative. For s-waves the predicted R^{ext} is too positive. To examine the sensitivity of the predictions to the depths of the surface potentials, we temporarily ignore the dispersion constraint and arbitrarily readjust the real and imaginary surface potentials for each partial wave to force very good agreement with the averaged scattering functions. Our criteria for $R^{ext}_{\ell j}(E)$ is that the model function (Eq. 23) give the best least-squares fit to the points in Fig. 6. Our criteria for the sum of reduced widths is that, when the integral (Eq. 22) is extended over the full domain, it agrees well with the empirical sum for the full domain. We choose the full domain in order to minimize the uncertainties that are inherent in a small sample of reduced widths. For p-waves, we can satisfy the two criteria by making independent adjustments in the real and imaginary surface potentials because there is little correlation in their effects on the real and imaginary parts of the complex R-function. This lack of correlation is related to the fact that the single-particle $2p_{1/2}$ and $2p_{3/2}$ states lie well below the resonance domain. The same independence does not hold for $s_{1/2}$ waves because the $3s_{1/2}$ state is only slightly unbound. Since the real and imaginary parts are not completely independent for s-waves, we adjust the surface potentials together to achieve the best overall fulfillment of the two criteria.

The resulting best-fit surface depths are presented in Fig. 2 at the center of the domain by a circle for s-waves and by solid points for p-waves. The heights of the symbols represent the uncertainties estimated from those shown in Figs. 6 and 7. The relative proximity of the circles and the points to the curves again demonstrates that the model predictions are fairly good. Specifically, the circles and points in Fig. 2a for the imaginary potential confirm that the strength of the potential decreases rapidly as the energy is reduced towards the Fermi energy and, in Fig. 2b, the circles and points confirm that the real dispersive term rises to near its maximum in the resonance region.

The most notable failure of the model as applied to the $n-^{40}Ar$ system is in fitting the total cross section for $2 < E < 11$ MeV. A similar inadequacy was obtained for the $n-^{40}Ar$ system. Despite the good agreement between predicted and experimental scattering functions, there is a hint of a parity dependence in the surface imaginary potential. Further studies are warranted in this regard for both isotopes. Analysis of the resonance region for ^{40}Ca has been initiated to investigate this feature.

VII. Code Development

For two years a code for calculating total cross sections in the R-matrix formalism has been used to obtain preliminary parameter estimates for use in a Bayesian-based fitting code. The code permitted rapid assessment of proposed spin and parity assignments for a given resonance through visual observation of peak cross section and asymmetry patterns. The value in this approach as opposed to use of the fitting code is in the rapid turn around possible on a dedicated microcomputer. Earlier versions of the code required an exit from the program in order to modify the parameter file before recalculation with new parameters. A major effort of the current reporting period has been the development of a graphical interface and least-squares fitting capability to the program. The former permits access to the parameter file from the screen and within the program, making possible an almost instantaneous screen update of any change made in the parameters of the resonance under investigation. Many repetitions are thus possible without leaving the program, speeding the preparation of a parameter file to be submitted to the Bayesian fitting code. During this process of development a means was found to perform χ^2 minimization without the calculation of partial derivatives with respect to all the varied parameters. This involved application of the downhill simplex method due to Nelder and Mead[11], implemented for multidimensional parameter variation. Variation of both resonance and R-external parameters is possible. Manual variation of any of the parameters is also possible from the screen through menu selection *via* mouse. This provides for a smoother and more efficient interaction with the data. With these additions to the basic calculation program it became straightforward to implement variation of the J^{π}-values. While this variation is not in the least-squares sense, it does permit automatic searching over a range of J^{π}-values. A record each χ^2 is stored for subsequent retrieval of best values. This option is not available in the Bayesian code and further refines the parameters and reduces the time required to obtain final parameters for a dataset. Finally in this regard, capability is implemented in the code for obtaining graphics output from dot-matrix or laser-printers, and a pen plotter. From the standpoint of published output in this period, this effort has not been productive but in terms of future analyses, the effort should prove worthwhile by reducing the time required to obtain a consistent set of resonance parameters for Bayesian refinement and by providing for a more quantitative and maximally informative interpretation of the total cross section data from ORELA. What was not feasible a few years ago on a microcomputer is now easily accomplished and is a favored approach

because of the interactive feature of the data analysis.

VIII. The n−^{48}Ca System

Previous analysis on this isotope was based on measurements of a scattering sample of 0.0577 atoms/barn of Ca which was 96% ^{48}Ca. Measurements were performed at the 200-m flight path of the ORELA facility. The high resolution total neutron cross sections were previously analyzed in the resolved region up to 2 MeV using the R-matrix formalism. The statistics at that time were not sufficient to extend beyond that energy without substantial ambiguity. Since then additional data have been taken which permit extension of the analysis to the limit of the inelastic threshold near 3.9 MeV. This has been facilitated by the spin-variation feature of the minimization code.

The previous analysis assumed a channel radius of 7.5 fm. This was chosen to be well outside the polarizing forces in order to permit the observed reduced widths to be compared to the single particle widths. The focus of the current analysis is to extend the analyzed region and to compare the deduced scattering functions with model scattering functions predicted by the dispersive optical model. We have chosen the channel radius for this analysis to be

$$a = 1.45 \cdot A^{1/3} = 5.27 \text{ fm}. \qquad 25$$

This will permit comparison to the very similar work on n−^{40}Ar, and minimize the interference of resonances with the large R-functions associated with the large radius. An additional consideration for the fitting relates to the fact that for the large-width $d_{5/2}$ resonances, the level shift of the R-matrix formalism is not constant over the resonance. For this reason we have set the boundary condition equal to the shift factor at the energy 1560 keV, i.e.,

$$B_{5/2} = S_{5/2}(1560 \text{ keV}). \qquad 26$$

Results of the analysis to an energy of 3.5 MeV are shown in Figs. 8−10 for selected regions. Large resonances due to $d_{5/2}$interaction dominate the structure up to 2.5 MeV, where $p_{3/2}$ strength begins to increase and become the dominant contributor.

IX. R-function Determinations

The interference between resonance and potential scattering are often sufficient to determine the R-function for a given partial wave when one has at least two resonances

separated sufficiently far in energy to ascertain the energy dependence of the interference. In the case of ^{48}Ca, conventional wisdom does not apply since the s- and p-wave resonances are small and thus do not manifest large interferences. The $d_{5/2}$ resonances on the other hand are so large that resonance-resonance interference dominates the resonance- potential scattering interference for all resonances of this J^{π} which are not remote from one of the large resonances. This results in larger uncertainties than normal on the R-functions. For the s- and p-wave R-functions we must resort to consideration of the off resonance scattering cross section in regions where two resonances of other J^{π} interfere. Since the partial wave cross section between two interfering resonances must go to zero, the remaining cross section must be provided by other partial waves through their R^{ext} parameters.

The resonances at 300, 400, and 450 keV are crucial for establishing the parameters of the R-function at lower energies. The J^{π}-values are clearly established by the peak cross sections. They are J = 1/2, 3/2, and 1/2, respectively, for the 300, 400, and 450 keV resonances. The large interference pattern with negative phase shows clearly that the 400-keV resonance is p-wave rather than d-wave because a d-wave resonance could not have such a large potential phase shift at these low energies. The other two resonances with J = 1/2 must be of opposite parity with one being p-wave and the other s-wave because of the different interference patterns observed. The one at 300 keV has a large phase shift while the o450-keV resonance shows essentially zero phase. The spin-orbit potential forces the $p_{1/2}$ potential phase to be more negative than that for the $p_{3/2}$. One can also argue that because the observed bound single-particle $p_{1/2}$ state is closer to the resonance region than the $p_{3/2}$ state, and there are no broad states observed for several MeV above the resonances. We therefore conclude that the 300-keV resonance must be $p_{1/2}$ and the 450-keV resonance must be $s_{1/2}$.

X. Average Proprerties

The parameters resulting from this analysis are reflected in the cumulative sum of reduced widths in Fig. 11 and the external R-functions shown in Fig. 12. There were only two resonances comfirmed as s-wave in the analysis. The $p_{1/2}$ and $p_{1/2}$ strength was small as was that for $d_{3/2}$. The $d_{5/2}$ strength was quite large. The previous analysis left open the question of the centroid of this strength. These results suggest that the peak has been reached due to the leveling of the sum of cumulative reduced widths as seen in Fig. 11 The $s_{1/2}$ level is unbound in this region and as a conseequence, only two s-wave resonances were observed in

the region. The $p_{1/2}$ and $p_{3/2}$ levels are unbound, the $p_{3/2}$ being nearer the separation energy. However the strenghs and R-functions are very little different for these partial waves. Most of the strength for the $d_{3/2}$ is attributable to a single resonance at 3400 keV. While this assignment is not unambiguous, an alternate assignment would require a major reconsideration of all spin assingnments of large resonances over the region 2600-3600 keV. The resonance provides peak height on which other resonances of higher J-value are superposed. This implies that no assignment of lower J-value would be sufficient. Alternately only the $f_{7/2}$ assignment might provide sufficient peak height without underlying structure. This does not however provide the needed asymmetry. The assignment is consistent with the level structure in this region. Residual interactions could be responsible for placing the $d_{5/2}$ level being nearer the separation energy than the $d_{3/2}$. We would otherwise expect to encounter strength in this shell at lower energies for the $d_{3/2}$ than for the $d_{5/2}$. One would need higher energy data to confirm this possible trend. A similar rapid increase of strength at onset was observed for $d_{5/2}$ in the $1 - 2$ MeV region.

The data provides evidence for f-wave interaction in the observed $f_{5/2}$ resonance at 2860 keV. This is confirmed by maximum peak height considerations. The $f_{7/2}$ assignment is ruled out by the fact that a width sufficiently large to fit the tails of the resonance results in an excessive peak height. We have not been able to make J^{π}- assignments for resonances of width comparable to the resolution width unless located near a large resonance of similar J^{π} with sufficient strength to produce significant asymmetry in the smaller resonance through resonance-resonance interference.

In order to consider the statistical properties of interest, we must be able to estimate the number of missed resonances in the analysis. An accurate measurement of the level spacings for each J^{π} is difficult because the levels widths smaller the the experimental resolution width may not be observed or may be assigned an incorrect J^{π}. To correct for missing levels we assume that the observed reduced widths are drawn from Porter-THomas (PT) distributions and that no resonances are missed with $\gamma^2_{\lambda n}$ greater than $< \gamma^2_{\lambda n} > /4$. To perform this test one forms a subset of resonances with given J^{π}, beginning with the largest $\gamma^2_{\lambda n}$, and successively includes the next smaller reduced width until the ratio of $< \gamma^2_{\lambda n} >$ to $<(\gamma^2_{\lambda n})^{1/2} >$ is the result expected for a sample obtained by drawing widths larger than $\frac{1}{4}$ the distribution mean from a PT distribution. The results of this test for the $d_{5/2}$ partial waves are shown in Fig. 13, where the histogram is the observed distribution and the solid curve is from the PT distribution deduced from the above test in which the histogram is fit for

$x \equiv (\gamma^2_{\lambda n})^{1/2} > (<\gamma^2_{\lambda n}>)^{1/2}/2$. From extrapolation of the solid curves to $x = 0$, in this and other similar curves for the other partial waves, we find the number missing, N^m, to be 1,8,0 and 0 for the $1/2^-$, $3/2^-$, $3/2^+$ and $5/2^+$ data sets, respectively. The solid curves are the expected distribution assuming no missed resonances.

These preliminary results are to be finalized and devoted to a dispersive optical model analysis before the end of the current reporting period. This will involve, as in the case of n– ^{40}Ar, the comparison of scattering functions and R-functions with model predictions for each individual partial wave. The model will use parameters deduced from extensive data on the n– ^{40}Ca system with suitable modification of the isovector potential for the different asymmetry coefficient.

Table I. Experimental energies and spectroscopic factors of particle and hole states for n− ^{40}Ar.

Particle states			Hole states		
$n\ell j$	E(MeV)	$(2j+1)S_n^-$	$n\ell j$	E(MeV)	$(2j+1)S_n^+$
$(f_{7/2})^2 + f_{7/2}$	−6.10	4.0	$(f_{7/2})^2 - f_{7/2}$	− 9.87	2.4
$2p_{3/2}$	−3.75	3.5	$1d_{3/2}$	−11.39	3.2
$2p_{1/2}$	−2.64	1.8	$2s_{1/2}$	−12.48	1.4

Figure Captions

Fig. 1. Experimental and predicted energies for levels in the valence shells for the $n-^{40}Ca$ and $n-^{40}Ar$ systems. Energies form Table I are represented by the EXPT structure for $n-^{40}Ar$.

Fig. 2. Imaginary (a) and real dispersive (b) surface potentials for $n-^{40}Ar$. The curves are for the model; the crosses represent the real dispersive depthsrequired to bind the $2s_{1/2}$, $1d_{3/2}$, $2p_{1/2}$, and $2p_{3/2}$ states exactly at the empirical energies in Table I. The open (solid) points show the surface depths required to fit the energy-averaged s-wave (p-wave) scattering functions in the resonance region.

Fig. 3. Neutron total cross section for ^{40}Ar. The points represent energy-averaged experimental cross sections and the curve is the predicted cross section from the dispersive optical model potential.

Fig. 4. Neutron total cross secton for ^{40}Ca. Both data points and the theoretical curve are form Ref. 4. The curve is the prediction of the optical model potential.

Fig. 5. Central depth of the symmetry potential in the Hartree-Fock approximation. The solid curve is derived from the differences between the $n-^{40}Ca$ and $n-^{40}Ar$ Hartree-Fock potentials, and the dashed curve was derived in Ref. 5 from the difference between $n-^{40}Ca$ and $n-^{208}Pb$ potentials. The vertical symbols show the uncertainties.

Fig. 6. Experimental and predicted external R-functions in the resonance energy domain. Experimental values are plotted as crosses for $s_{1/2}$, circles for $p_{1/2}$ and points for $p_{3/2}$ partial waves. The predicted curves are solid for $s_{1/2}$, short-dash for $p_{1/2}$ and long-dash for $p_{3/2}$ partial waves. The R-function expansions used a 5.0 fm channel radius.

Fig. 7. Sums of experimental reduced neutron widths and integrals of theoretical strength functions for the $s_{1/2}$, $p_{1/2}$, and $p_{3/2}$ neutron partial waves for ^{40}Ar in the resonance region. The error bars show the uncertainties in the full sums for an assumed Porter-Thomas distribution of widths. The curve represents integrals up to the energy of the strength functions from the model.

Fig. 8. Total cross section for $n-^{48}Ca$ over the neutron energy range 1.2–2.2 MeV. The short-, intermediate-, and long-dash lines betoken the contributions due to $p_{1/2}$, $p_{3/2}$ and $d_{5/2}$ partial waves, respectively. The solid line through the data points represents the sum of all partial waves.

Fig. 9. Total cross section for $n-^{48}Ca$ over the neutron energy range 2.0−3.0 MeV. The short-, intermediate-, and long-dash lines betoken the contributions due to $p_{1/2}$, $d_{3/2}$ and $d_{5/2}$ partial waves, respectively. The solid line through the data points represents the sum of all partial waves.

Fig. 10. Total cross section for $n-^{48}Ca$ over the neutron energy range 2.9−3.5 MeV. The short-, intermediate-, and long dash lines betoken the contributions due t $p_{1/2}$, $d_{3/2}$ and $d_{5/2}$ partial waves, respectively. The solid line through the data points represents the sum of all partial waves. The solid partial wave curve corresponds to $p_{3/2}$.

Fig. 11. Cumulative sum of reduced widths for p- and d-wave resonances observed in $n-^{48}Ca$.

Fig. 12. The external R-functions for ^{48}Ca over the neutron energy range 0 − 4.0 MeV.

Fig. 13. Porter-Thomas test for missing resonances for $d_{5/2}$ resonances. The histogram represents the number of resonances with $(\gamma_\lambda^2)^{1/2}$ greater than the abscissa. The dashed curve corresponds to results expected if widths are drawn from a Porter-Thomas distribution assuming no levels are missed. The solid curve is for 4-missing resonances.

REFERENCES

1 C.H. Johnson and C. Mahaux, Phs. Rev. C, 37, 2589(1989).

2 J.P Delaroche, Y. Wang and J. Rapaport (unpublished).

3 C.H. Johnson, D.J. Horen and C. Mahaux, Phys. Rev. C, 36, 2252(1987).

4 C.H. Johnson and C. Mahaux, Phys. Rev. C, 38, 2589(1988).

5 P.M. Endt and C. Van der Leun, Nucl. Phys. A310, 1(1978).

6 R.R. Winters, R.F. Carlton, N.W. Hill and C.H. Johnson, Phys. Rev. C, 41.

7 L.J. Satkowiak, S.M. Ferguson, R.E. Shamu and M. Soga, Phys. Lett. 175, 266(1985).

8 J.F. Tonn, R.E. Segel, J.A. Nolen, W.S. Chien and P.T. Debevec, Phys. Rev. C, 16, 1357(1977).

9 C.H. Johnson, D.J. Horen and C. Mahaux, Phys. Rev. C, 36, 2252(1987).

10 C.H. Johnson, C. Mahaux and R.R. Winters, Phys. Rev. C, 32, 359(1985).

11 J.A. Nelder and R. Mead, Computer Journal 7 , 308 (1965).

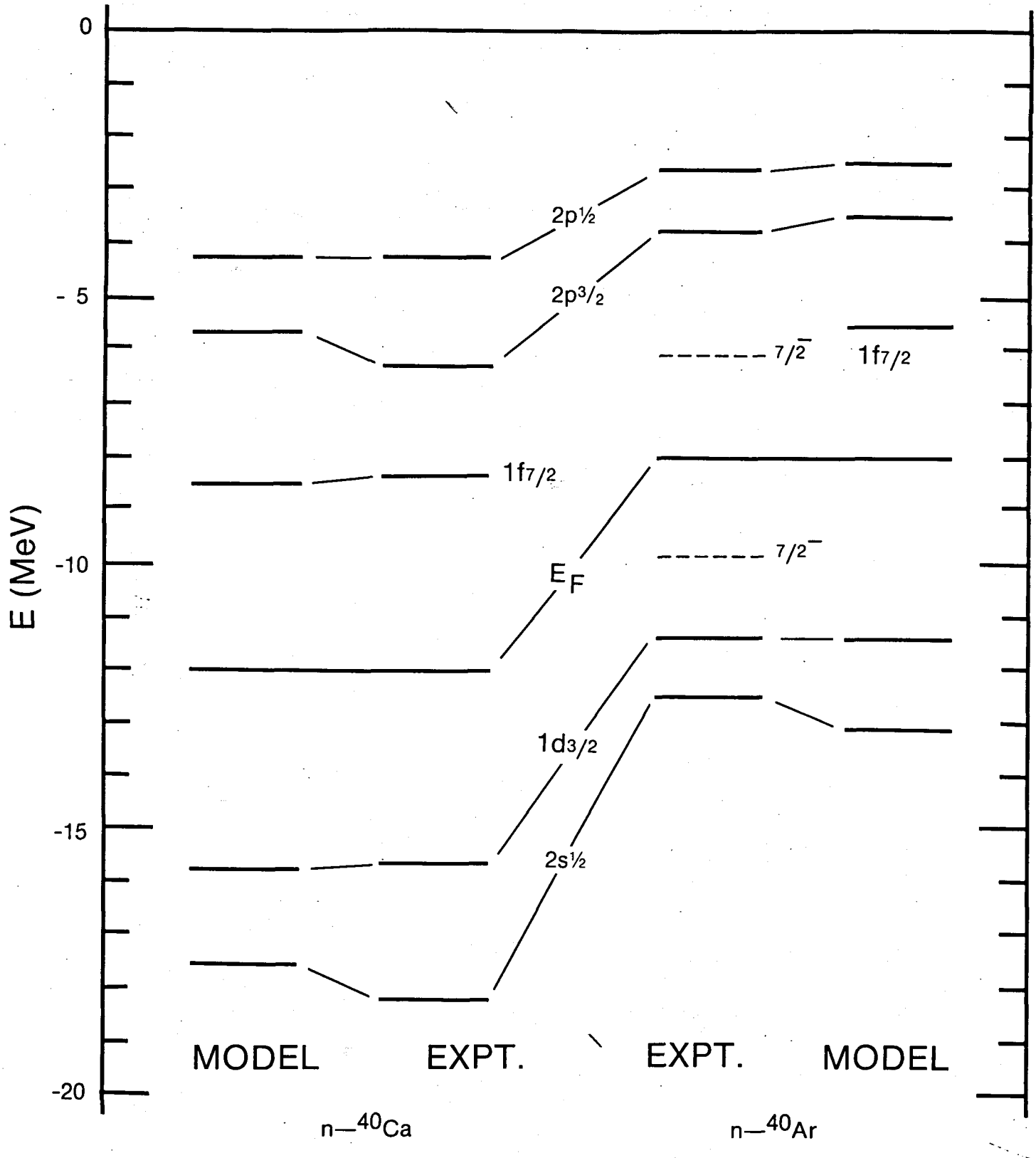
0
- 5
-10
-15
-20
E (MeV)
2p½
2p3/2
7/2⁻
1f7/2
1f7/2
7/2⁻
EF
1d3/2
2s½
MODEL
EXPT.
EXPT.
MODEL
n—40Ca
n—40Ar

Figure 1

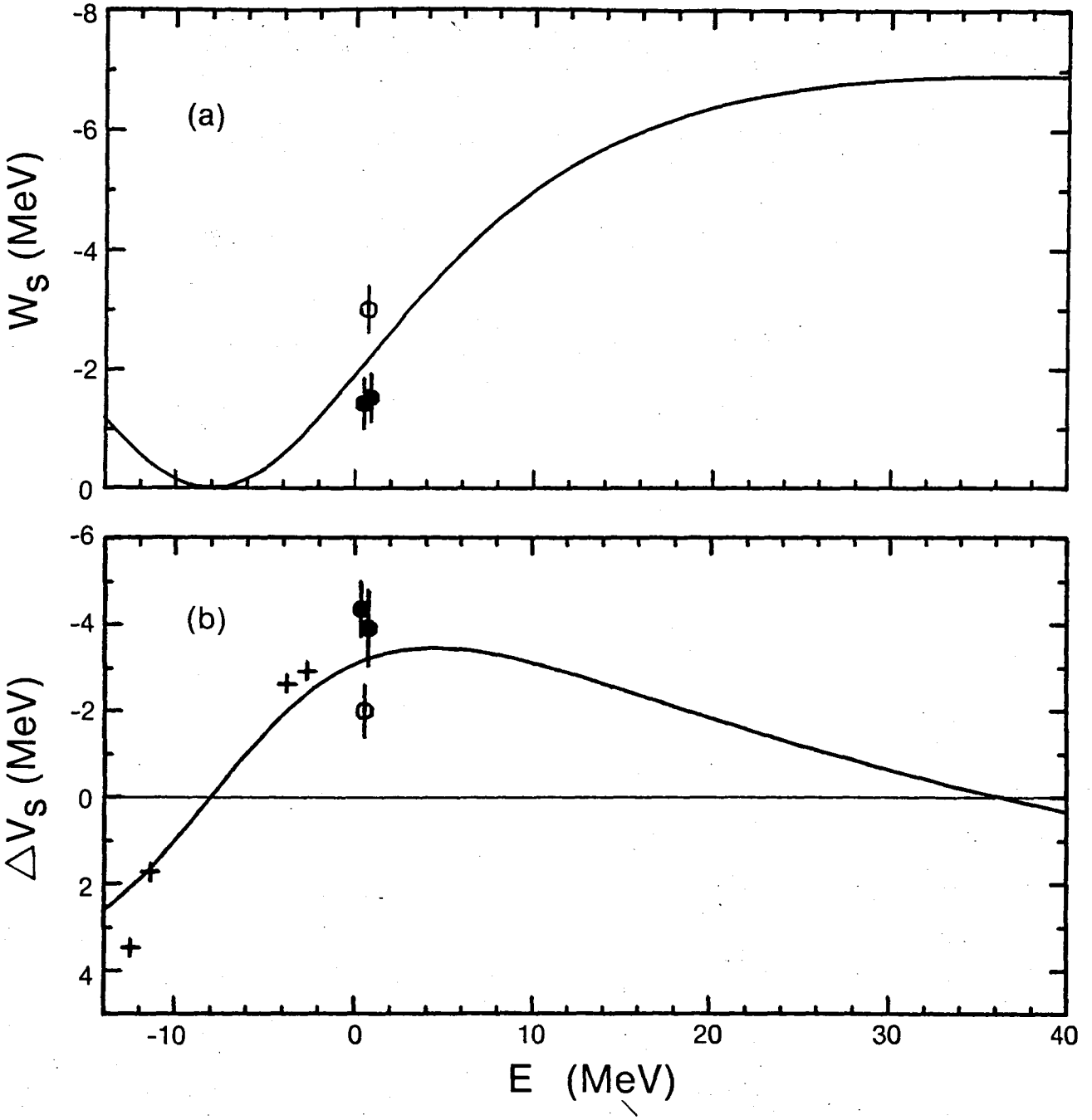

Figure 2

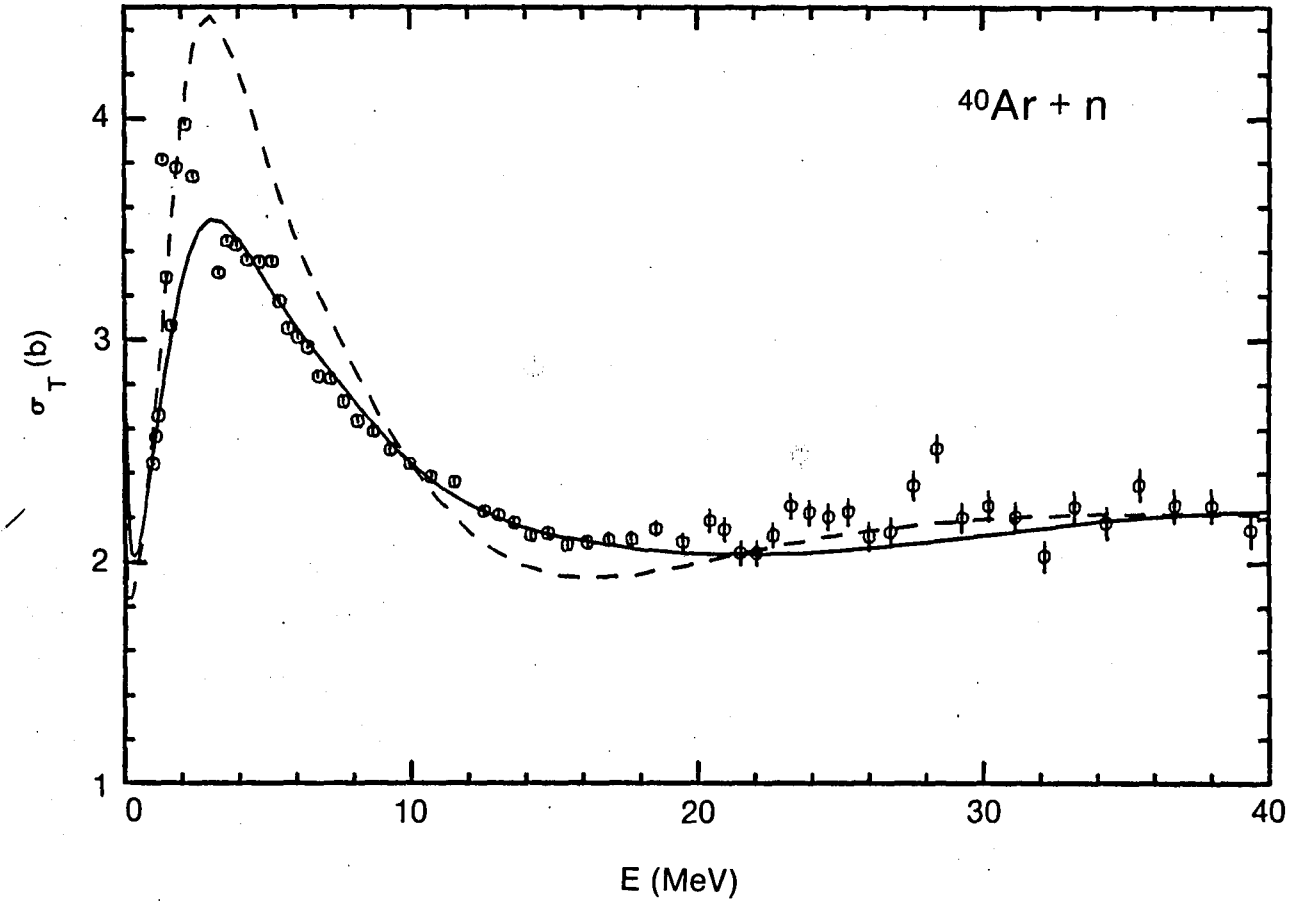

Figure 3

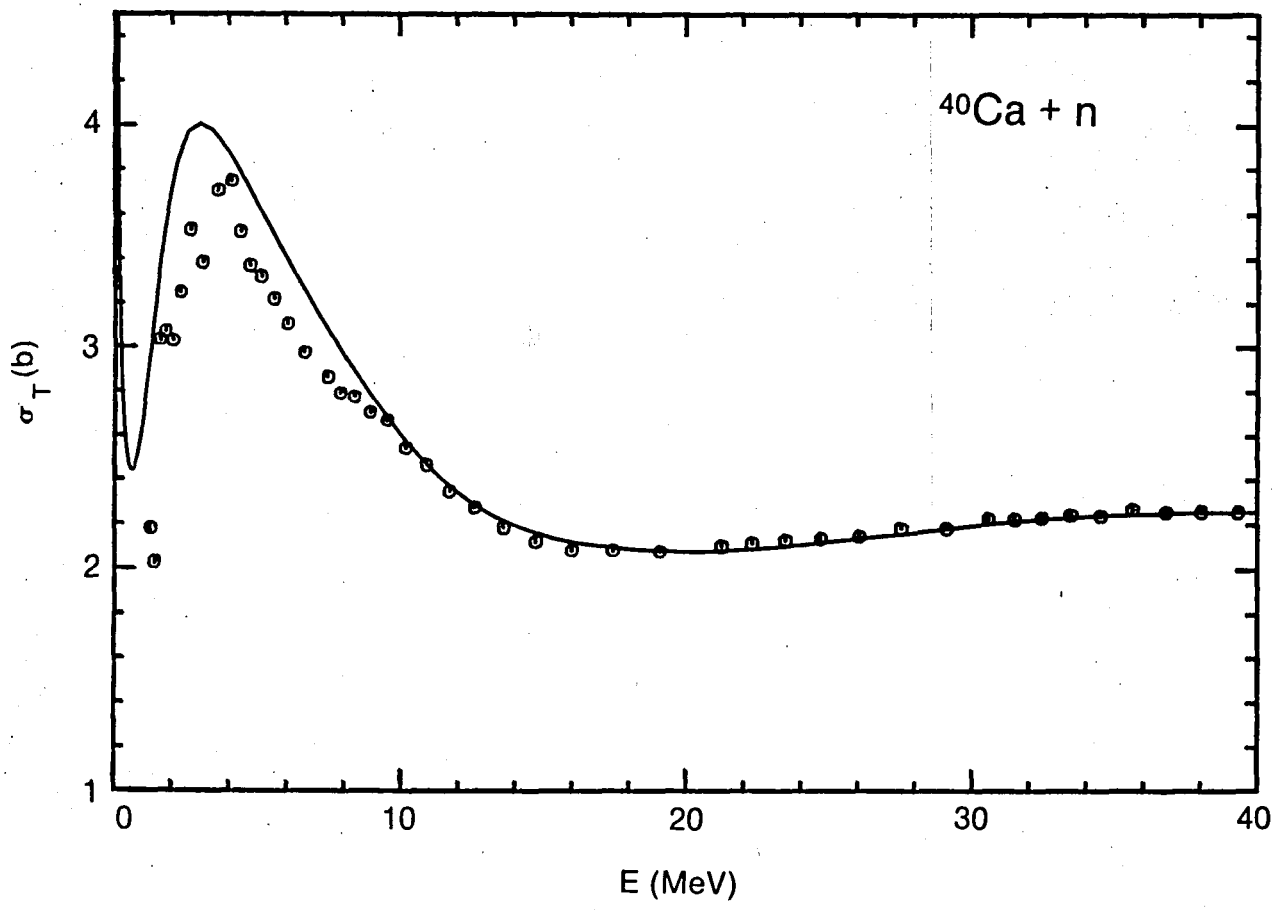

Figure 4

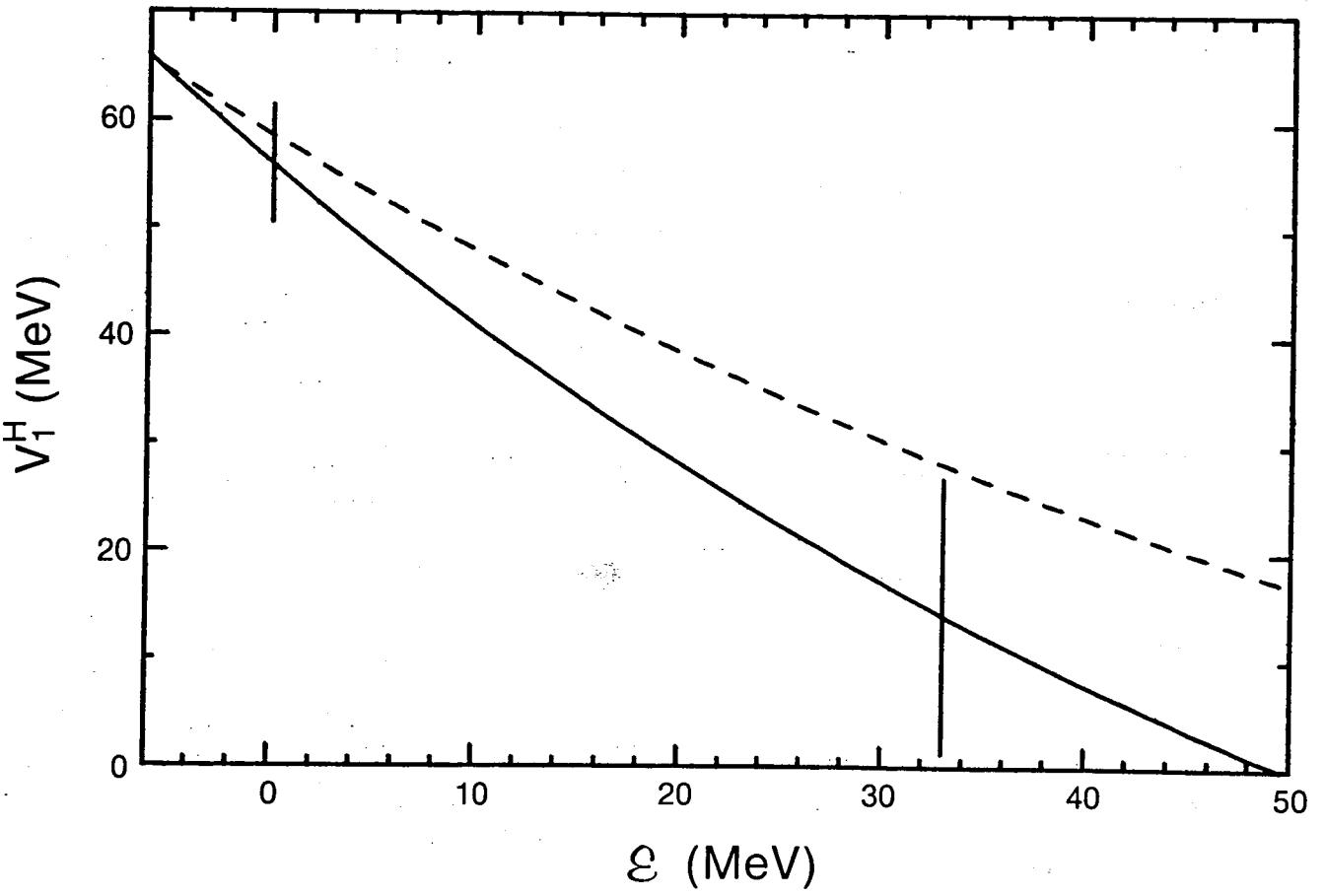

Figure 5

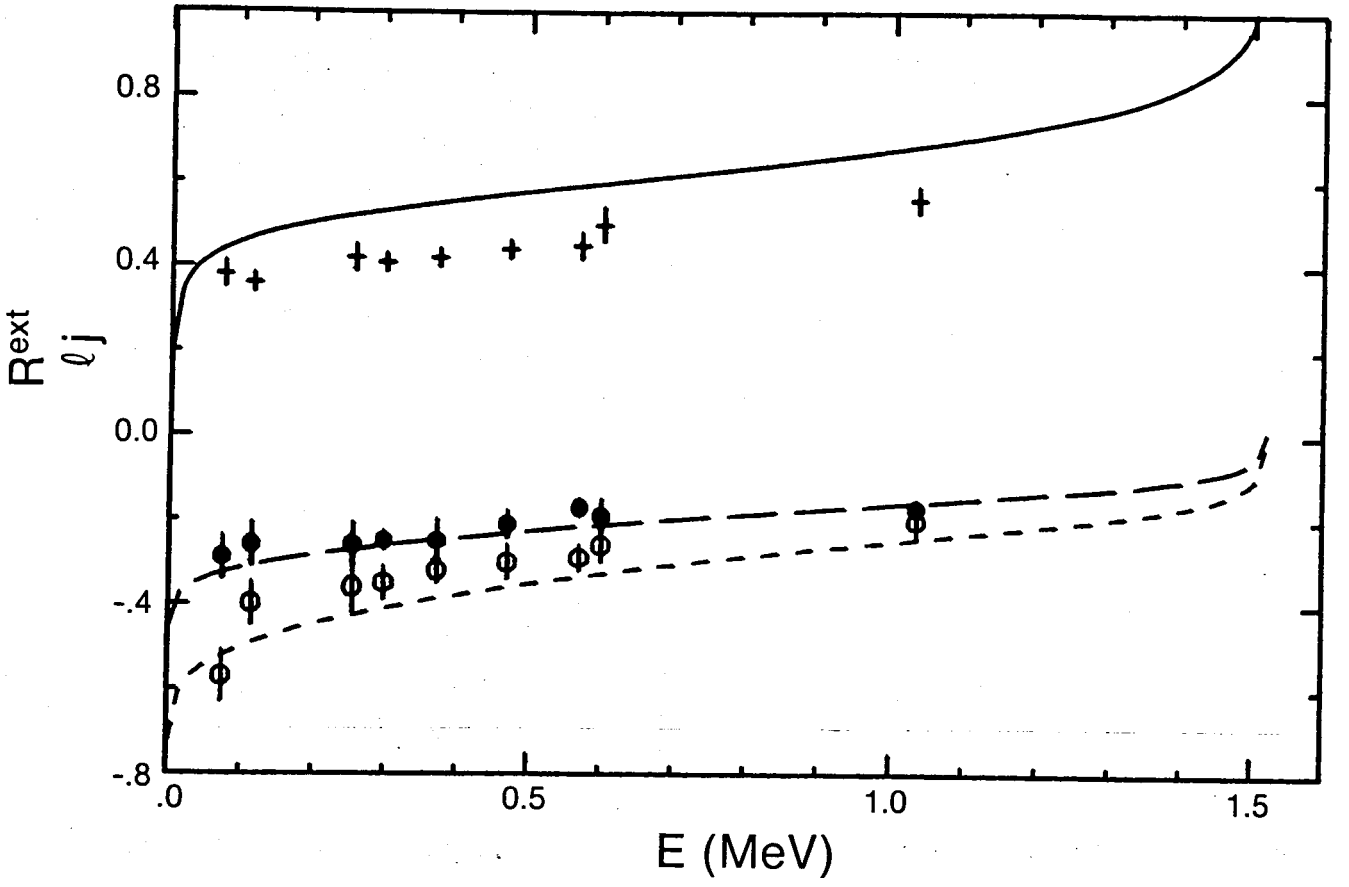

Figure 6

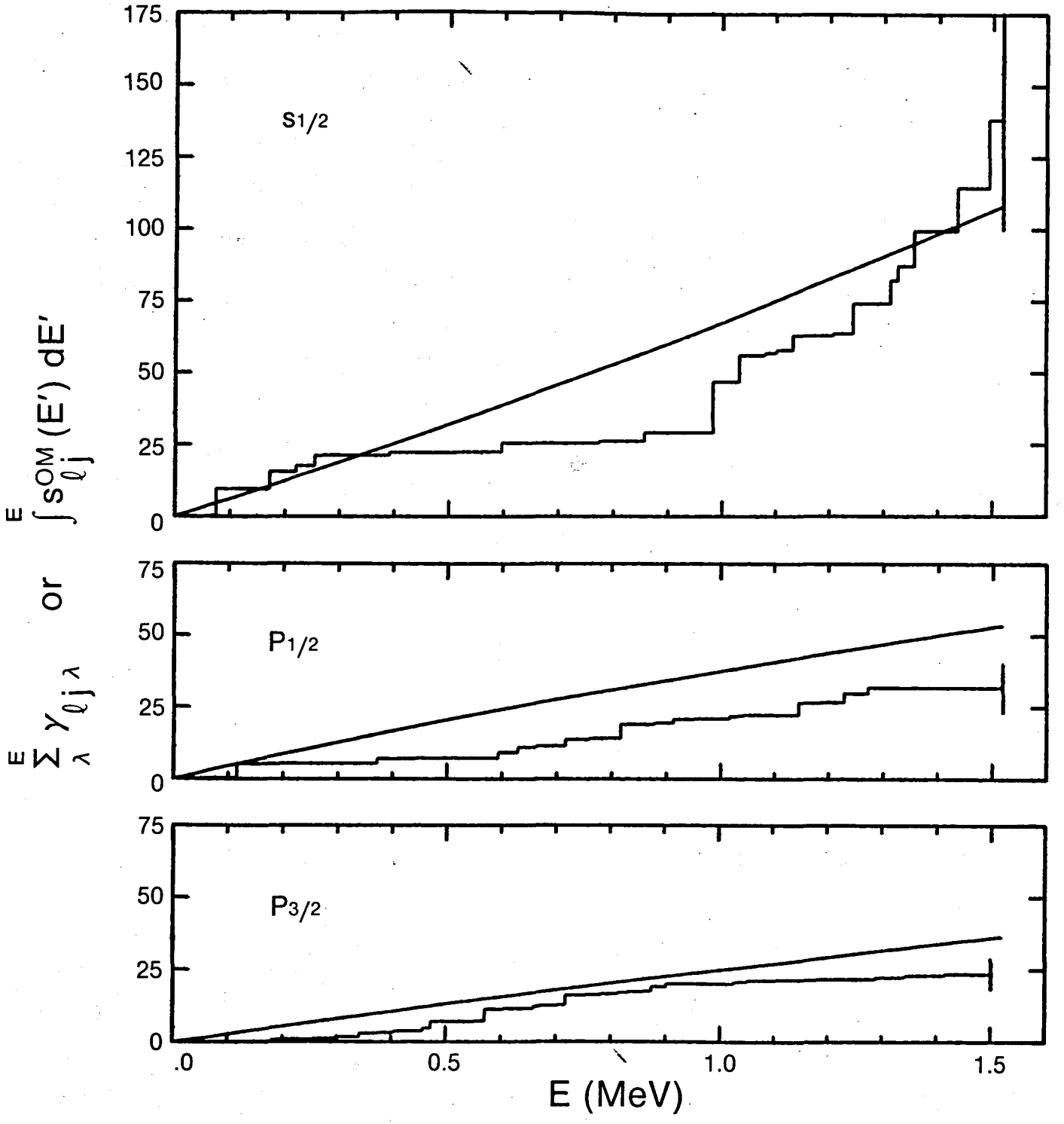
175
150
125
100
75
50
25
0
S1/2
$\int_0^E s_{\ell j}^{OM}(E')\,dE'$
or
$\sum_\lambda^E \gamma_{\ell j \lambda}$
75
50
25
0
P1/2
75
50
25
0
P3/2
.0
0.5
1.0
1.5
E (MeV)

Figure 7

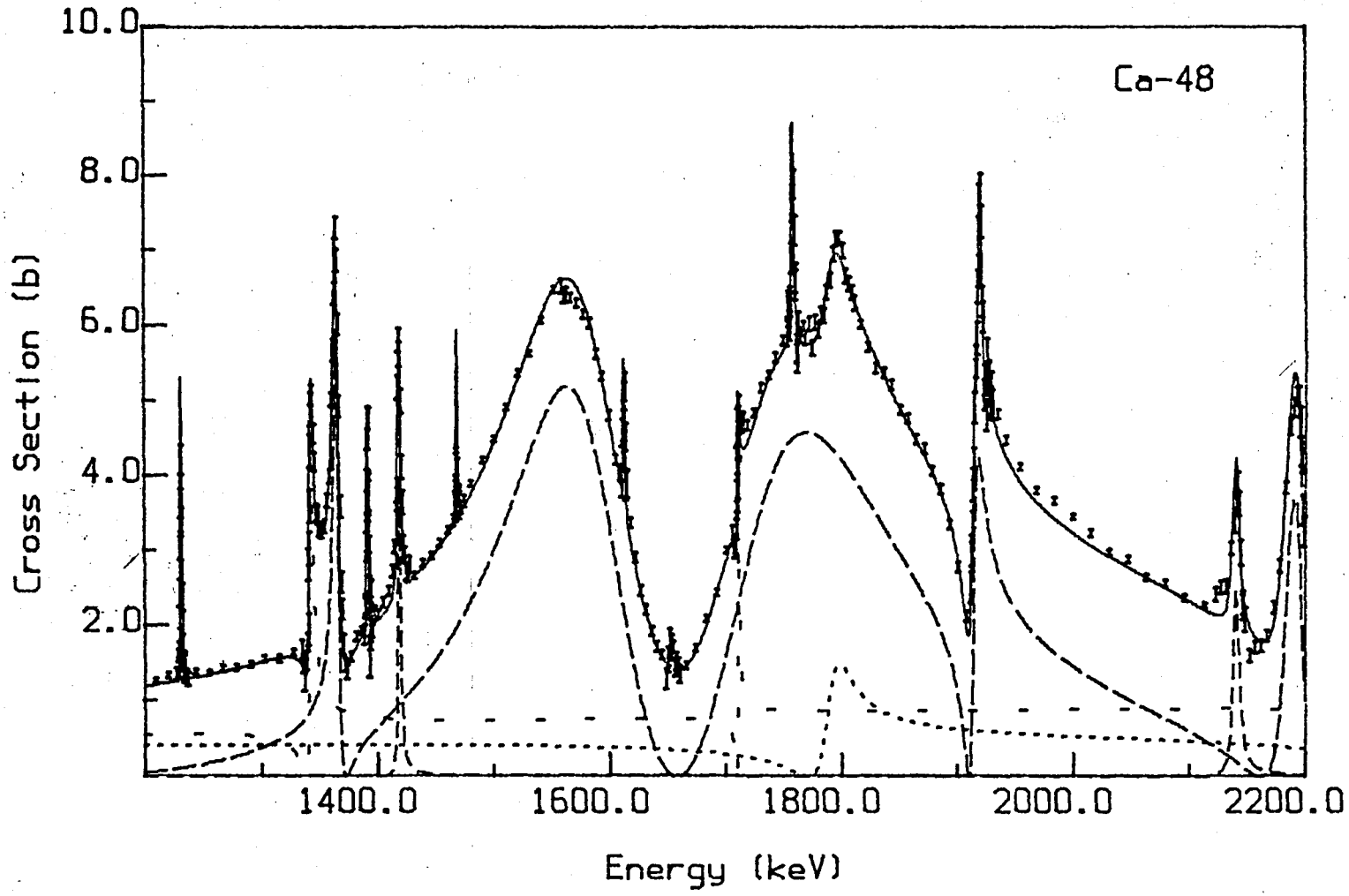
Ca-48
Cross Section (b)
10.0
8.0
6.0
4.0
2.0
1400.0
1600.0
1800.0
2000.0
2200.0
Energy (keV)

Figure 8

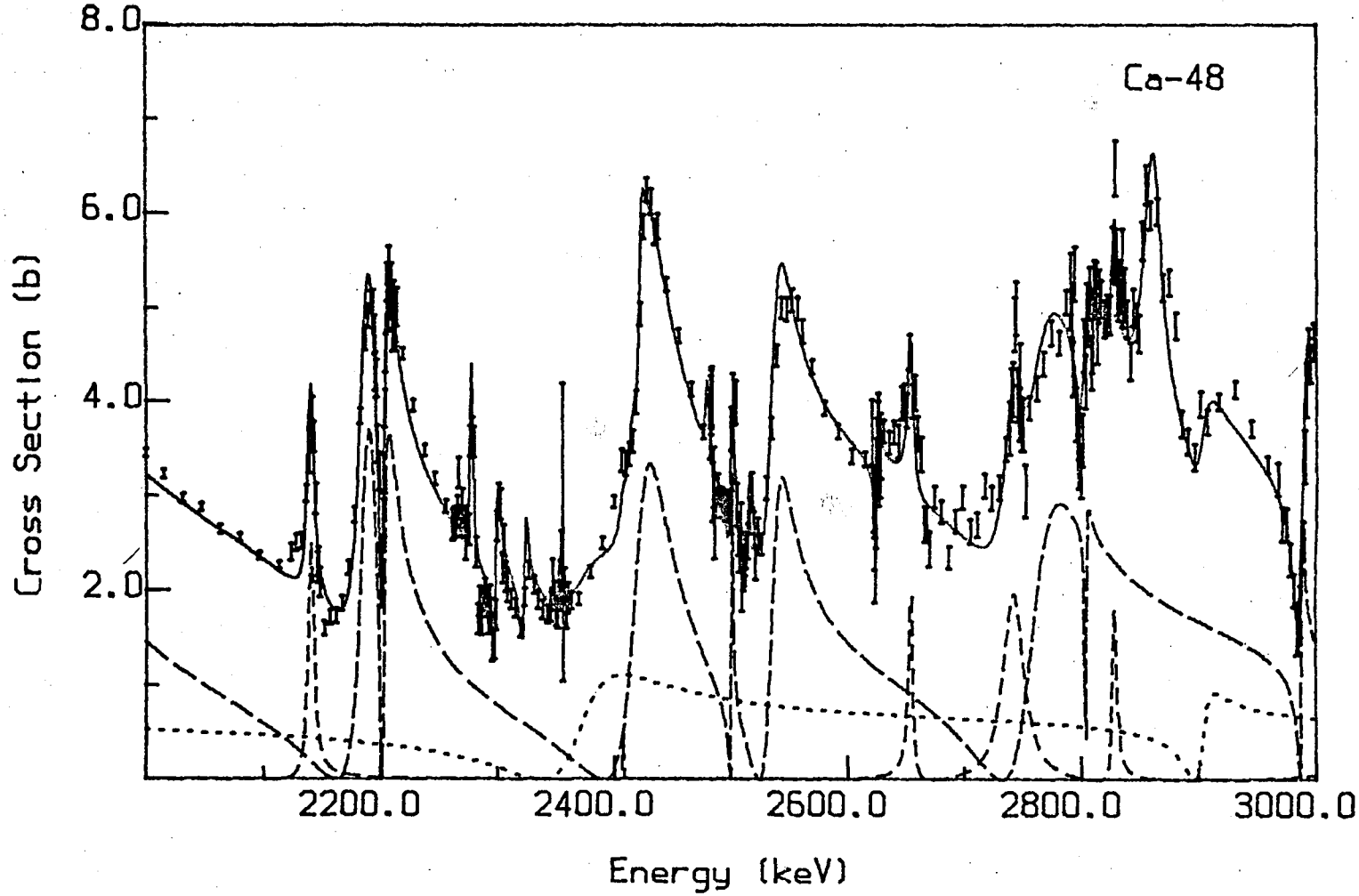
Ca-48
Cross Section (b)
8.0
6.0
4.0
2.0
2200.0
2400.0
2600.0
2800.0
3000.0
Energy (keV)

Figure 9

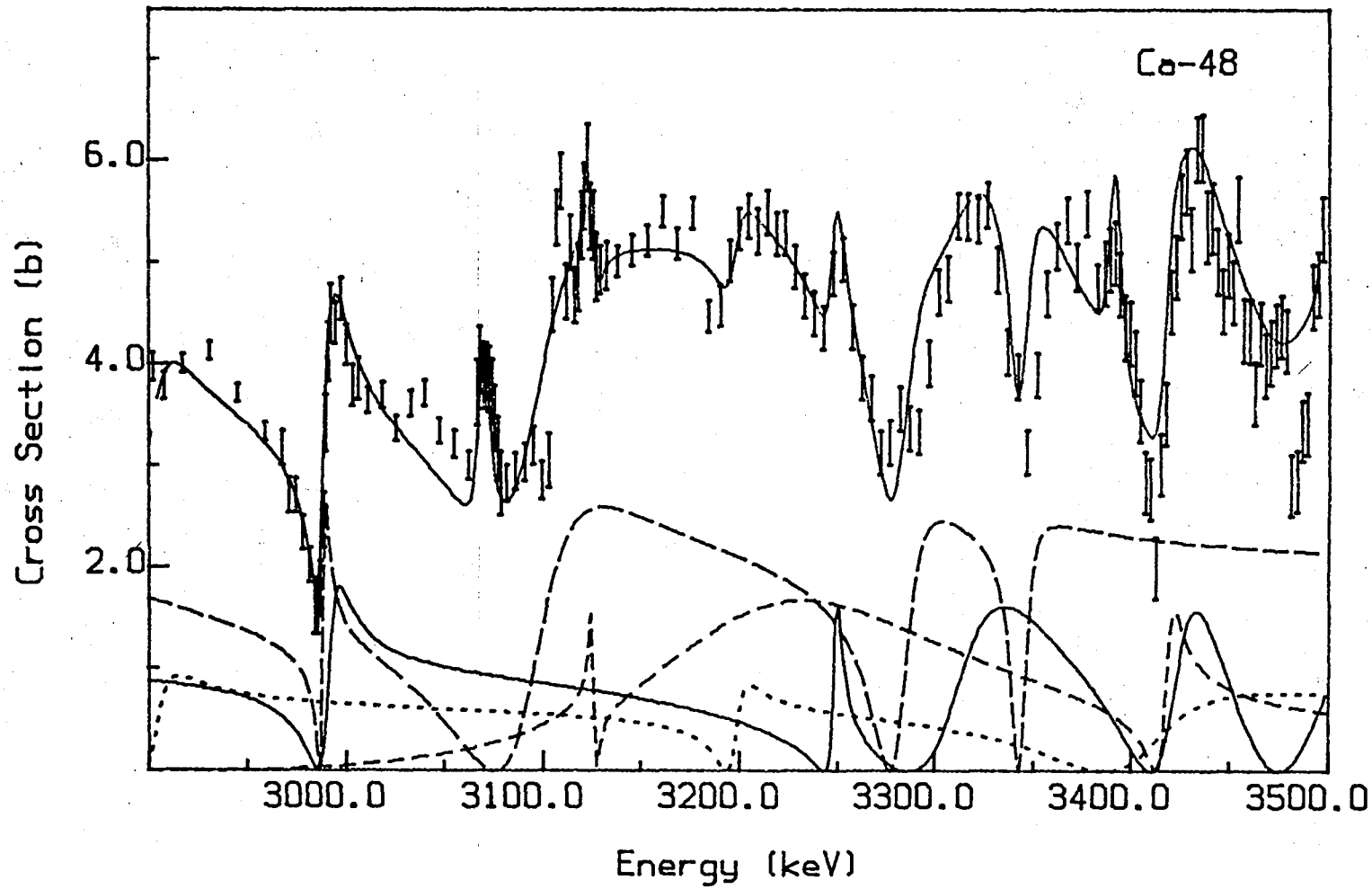
Ca-48
Cross Section (b)
6.0
4.0
2.0
3000.0
3100.0
3200.0
3300.0
3400.0
3500.0
Energy (keV)

Figure 10

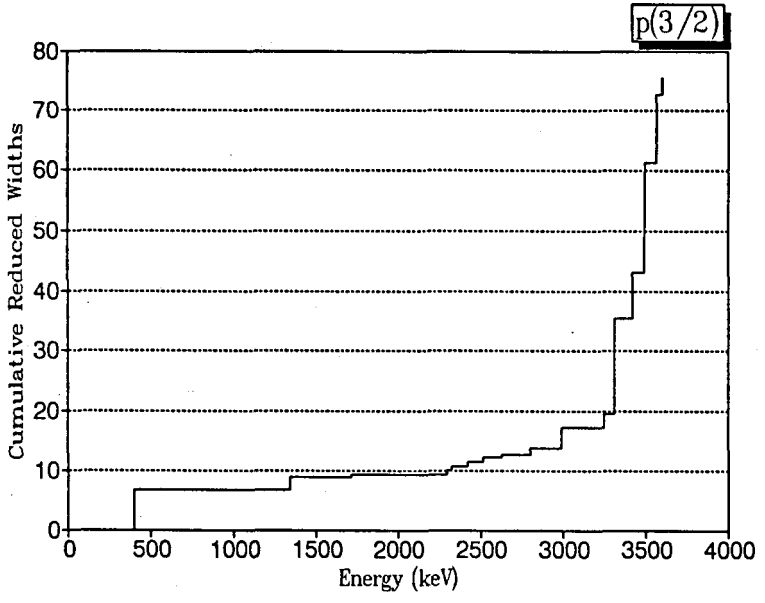
p(3/2)
Cumulative Reduced Widths
Energy (keV)
0
10
20
30
40
50
60
70
80
0
500
1000
1500
2000
2500
3000
3500
4000

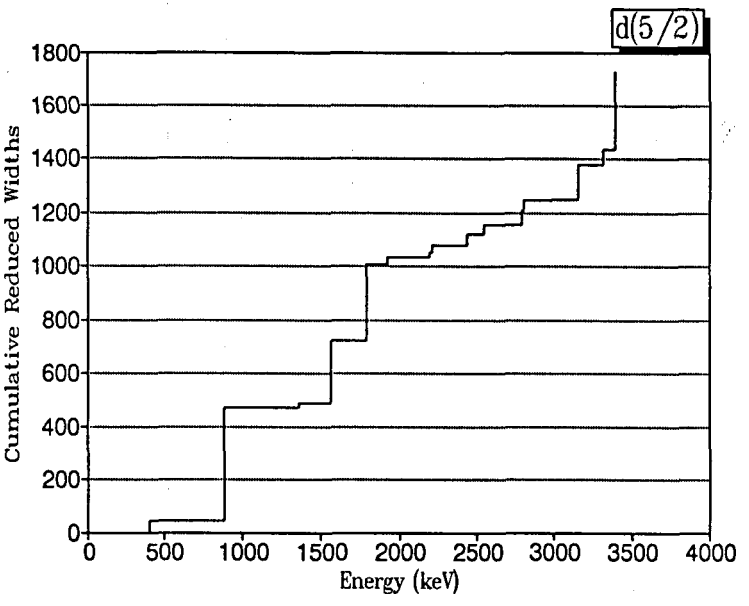
d(5/2)
Cumulative Reduced Widths
Energy (keV)
0
200
400
600
800
1000
1200
1400
1600
1800
0
500
1000
1500
2000
2500
3000
3500
4000

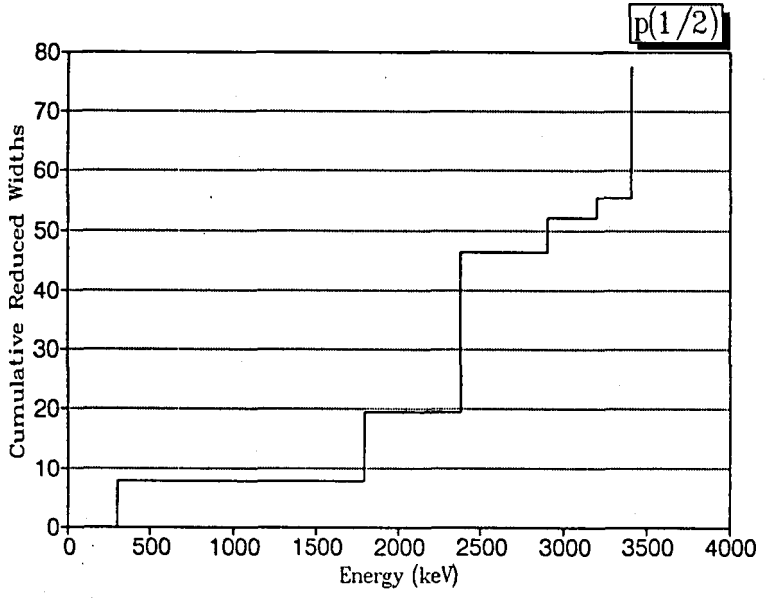
p(1/2)
Cumulative Reduced Widths
Energy (keV)
0
10
20
30
40
50
60
70
80
0
500
1000
1500
2000
2500
3000
3500
4000

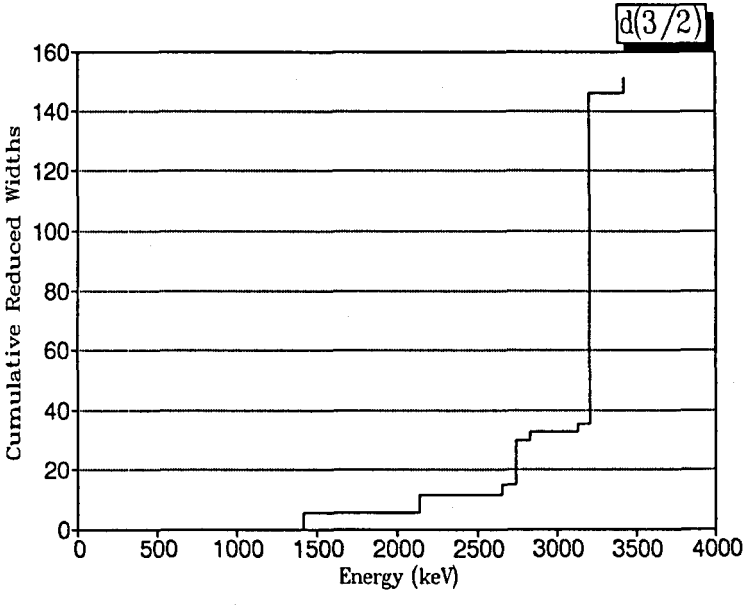
d(3/2)
Cumulative Reduced Widths
Energy (keV)
0
20
40
60
80
100
120
140
160
0
500
1000
1500
2000
2500
3000
3500
4000

Figure 11

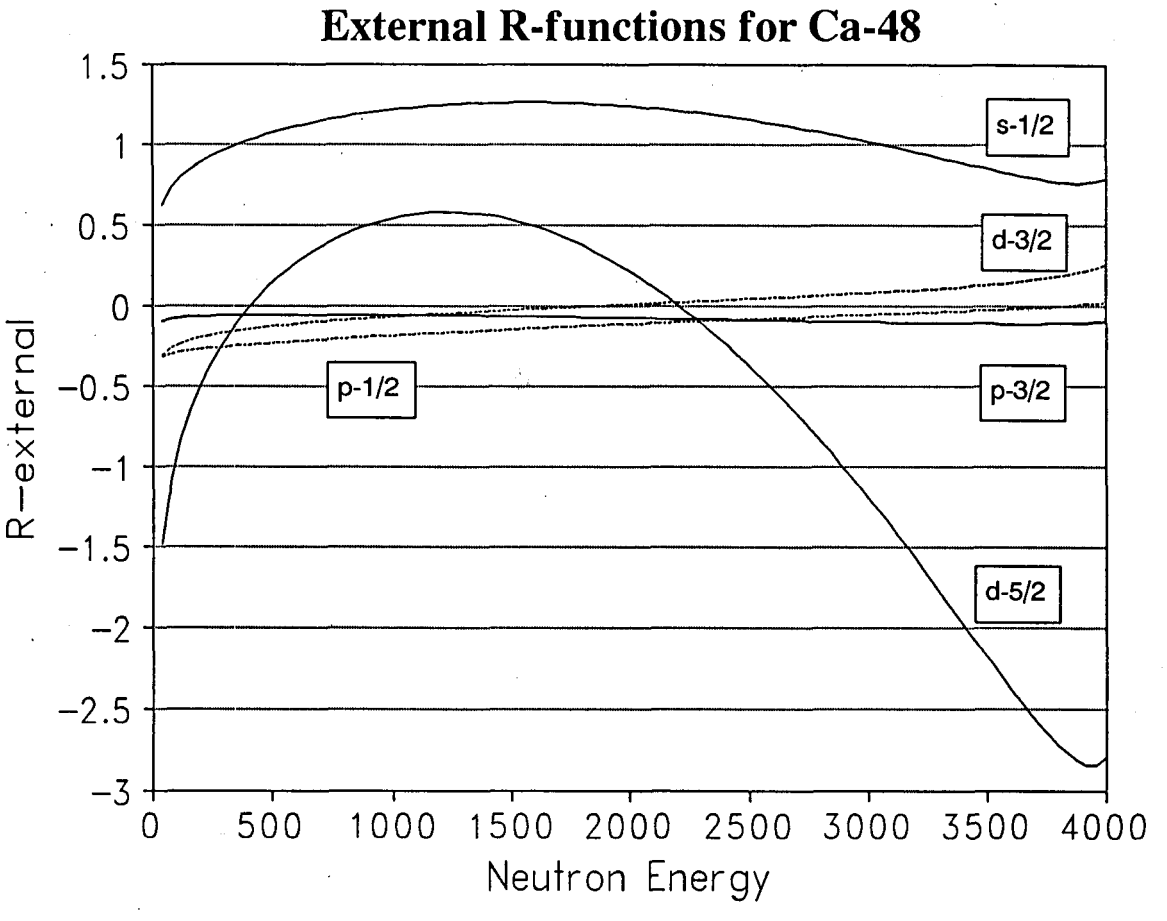
External R-functions for Ca-48
1.5
1
0.5
0
−0.5
−1
−1.5
−2
−2.5
−3
R−external
0
500
1000
1500
2000
2500
3000
3500
4000
Neutron Energy
s-1/2
d-3/2
p-1/2
p-3/2
d-5/2

Figure 12

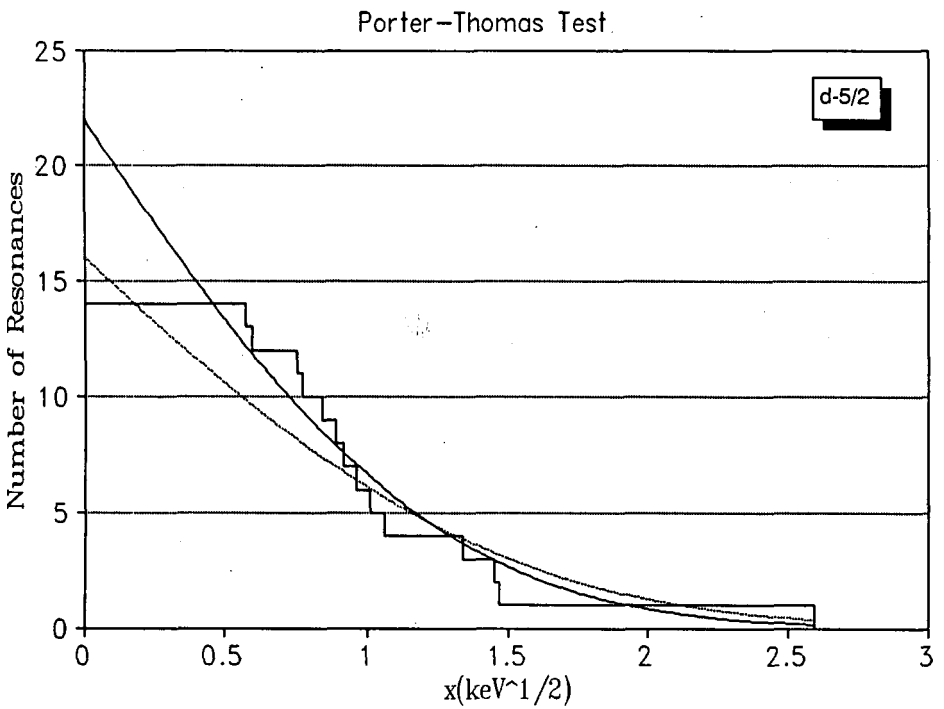
Porter–Thomas Test
d-5/2
Number of Resonances
25
20
15
10
5
0
0
0.5
1
1.5
2
2.5
3
x(keV^1/2)

Figure 13